PROBING THE INNERMOST REGIONS OF AGN JETS AND THEIR MAGNETIC FIELDS WITH *RADIOASTRON*. I. IMAGING BL LACERTAE AT 21 μas RESOLUTION

JOSÉ L. GÓMEZ[1], ANDREI P. LOBANOV[2,3], GABRIELE BRUNI[2], YURI Y. KOVALEV[2,4], ALAN P. MARSCHER[5], SVETLANA G. JORSTAD[5,6], YOSUKE MIZUNO[7], UWE BACH[2], KIRILL V. SOKOLOVSKY[4,8,9], JAMES M. ANDERSON[2,10], PABLO GALINDO[1], NIKOLAY S. KARDASHEV[4], AND MIKHAIL M. LISAKOV[4]

[1] Instituto de Astrofísica de Andalucía-CSIC, Glorieta de la Astronomía s/n, E-18008 Granada, Spain; jlgomez@iaa.csic.es
[2] Max-Planck-Institut für Radioastronomie, Auf dem Hügel 69, D-53121 Bonn, Germany
[3] Institut für Experimentalphysik, Universität Hamburg, Luruper Chaussee 149, D-22761 Hamburg, Germany
[4] Astro Space Center, Lebedev Physical Institute, Russian Academy of Sciences, Profsoyuznaya str. 84/32, Moscow 117997, Russia
[5] Institute for Astrophysical Research, Boston University, 725 Commonwealth Avenue, Boston, MA 02215, USA
[6] Astronomical Institute, St. Petersburg State University, Universitetskij Pr. 28, Petrodvorets, 198504 St. Petersburg, Russia
[7] Institute for Theoretical Physics, Goethe University, D-60438, Frankfurt am Main, Germany
[8] Sternberg Astronomical Institute, Moscow State University, Universitetskii pr. 13, 119992 Moscow, Russia
[9] Institute of Astronomy, Astrophysics, Space Applications and Remote Sensing, National Observatory of Athens, Vas. Pavlou & I. Metaxa, GR-15 236 Penteli, Greece
[10] Helmholtz-Zentrum Potsdam, Deutsches GeoForschungsZentrum GFZ, Telegrafenberg, D-14473 Potsdam, Germany

ABSTRACT

We present the first polarimetric space very long baseline interferometry (VLBI) imaging observations at 22 GHz. BL Lacertae was observed in 2013 November 10 with the *RadioAstron* space VLBI mission, including a ground array of 15 radio telescopes. The instrumental polarization of the space radio telescope is found to be less than 9%, demonstrating the polarimetric imaging capabilities of *RadioAstron* at 22 GHz. Ground–space fringes were obtained up to a projected baseline distance of 7.9 Earth diameters in length, allowing us to image the jet in BL Lacertae with a maximum angular resolution of 21 μas, the highest achieved to date. We find evidence for emission upstream of the radio core, which may correspond to a recollimation shock at about 40 μas from the jet apex, in a pattern that includes other recollimation shocks at approximately 100 and 250 μas from the jet apex. Polarized emission is detected in two components within the innermost 0.5 mas from the core, as well as in some knots 3 mas downstream. Faraday rotation analysis, obtained from combining *RadioAstron* 22 GHz and ground-based 15 and 43 GHz images, shows a gradient in rotation measure and Faraday-corrected polarization vector as a function of position angle with respect to the core, suggesting that the jet in BL Lacertae is threaded by a helical magnetic field. The intrinsic de-boosted brightness temperature in the unresolved core exceeds 3×10^{12} K, suggesting, at the very least, departure from equipartition of energy between the magnetic field and radiating particles.

Key words: galaxies: active – galaxies: individual (BL Lac) – galaxies: jets – polarization – radio continuum: galaxies

1. INTRODUCTION

The accretion of gas onto the supermassive black holes lurking at the center of active galactic nuclei (AGNs) gives rise to powerful relativistic jets (e.g., Marscher et al. 2002). These are produced by dynamically important magnetic fields twisted by the differential rotation of the black hole's accretion disk or ergosphere (Blandford & Znajek 1977; Blandford & Payne 1982; McKinney & Blandford 2009; Zamaninasab et al. 2014). Observational signatures for the existence of such helical magnetic fields can be obtained by looking for Faraday rotation gradients, produced by the systematic change in the net line-of-sight magnetic field component across the jet width (Laing 1981; Asada et al 2002).

Obtaining a better understanding of the jet formation, and of the role played by the magnetic field, requires probing the innermost regions of AGN jets, but this is limited by the insufficient angular resolution provided by existing, ground-based, very long baseline interferometry (VLBI) arrays. However, space VLBI, in which one of the antennas is in Earth's orbit, is capable of extending the baseline distances beyond the Earth's diameter, reaching unprecedentedly high angular resolutions in astronomical observations (e.g., Levy

et al. 1986; Gómez & Marscher 2000; Gabuzda & Gómez 2001; Lobanov & Zensus 2001).

On 2011 July 18, the *RadioAstron* space VLBI mission (Kardashev et al. 2013) began to operate, featuring a 10 m space radio telescope (SRT) on board the satellite *Spektr-R*. *RadioAstron* provides the first true full-polarization capabilities for space VLBI observations on baselines longer than the Earth's diameter at 0.32, 1.6, and 22 GHz. The SRT also operates at 5 GHz, but an on board hardware failure limits the recording mode at this frequency to left circular polarization only.

The current paradigm for AGNs is that their radio emission is explained by synchrotron radiation from relativistic electrons that is Doppler boosted through bulk motion. In this model, the intrinsic brightness temperatures cannot exceed 10^{11}–10^{12} K (Kellermann & Pauliny-Toth 1969; Readhead 1994). Typical Doppler boosting is expected to be able to raise this temperature by a factor of ~10 (see also Hovatta et al. 2009; Lister et al. 2013). For direct interferometric measurements, increasing the interferometer baseline length is the only way to measure higher brightness temperatures (see, e.g., Kovalev et al. 2005), and hence, to place stringent observational constraints on the physics of the most energetic relativistic

outflows. The highest observing frequency, 22 GHz, and resolution of *RadioAstron* allow us to probe the most energetic regions located close to the central engine (see, e.g., Lobanov 1998; Sokolovsky et al. 2011; Pushkarev et al. 2012) while scattering effects in the Galaxy are negligible (Pushkarev & Kovalev 2015).

First polarimetric space VLBI imaging observations with *RadioAstron* were performed on 2013 March 9 during the early science program, targeting the high-redshift quasar TXS 0642 +449 at a frequency of 1.6 GHz (Lobanov et al. 2015). Instrumental polarization of the SRT was found to be smaller than 9% in amplitude, demonstrating the polarimetric imaging capabilities of *RadioAstron* at this frequency (see also Pashchenko et al. 2015). Fringes on ground–space baselines were found up to projected baseline distances of 6 Earth diameters in length, allowing for imaging of 0642+449 with an angular resolution of 0.8 mas—a four-fold improvement over ground VLBI observations at this frequency.

In this paper, we present the first polarimetric space VLBI imaging observations at 22 GHz, obtained as part of our *RadioAstron* Key Science Program (KSP), aimed to develop, commission, and exploit the unprecedented high angular resolution polarization capabilities of *RadioAstron* to probe the innermost regions of AGN jets and their magnetic fields. A sample of powerful, highly polarized, and γ-ray emitting blazars is being observed within our KSP, including several quasars, BL Lac objects, and radio galaxies. In this first paper of a series containing our *RadioAstron* KSP results, we present our observations of BL Lacertae, the eponymous blazar that gives name to the class of BL Lac objects.

The jet of BL Lac is pointing at us with a viewing angle of $\sim 8°$ with bulk flow at a Lorentz factor of ~ 7 (Jorstad et al. 2005). Previous observations have revealed a multi-wavelength outburst, from radio to γ-rays, triggered by the passing of a bright moving feature through a standing shock associated with the core of the jet (Marscher et al. 2008). Rotation of the optical polarization angle prior to the γ-ray flare led Marscher et al. (2008) to conclude that the acceleration and collimation zone, upstream of the radio core, is threaded by a helical magnetic field. The existence of a helical magnetic field in BL Lac has also been suggested by Cohen et al. (2015) through analysis of the MOJAVE monitoring program data. These authors claim that Alfvén waves triggering the formation of superluminal components are excited by changes in the position angle of a recollimation shock (located at a distance from the core of ~ 0.26 mas), in a similar way as found in magnetohydrodynamical simulations of relativistic jets threaded by a helical magnetic field (Lind et al. 1989; Meier 2013).

VLBA monitoring programs at 43 GHz have revealed the existence of a second stationary feature besides the one described previously at 0.26 mas, located at a distance of ~ 0.1 mas (Jorstad et al. 2005). Variations in the position angle of these innermost components suggest that the jet in BL Lac may be precessing (Stirling et al. 2003; Mutel & Denn 2005).

Faraday rotation analysis reveals a variable rotation measure (RM) in the core of BL Lac, including sign reversals. Observations by Zavala & Taylor (2003) give -376 rad m^{-2}, while O'Sullivan & Gabuzda (2009) find RM values between -1000 and $+240$ rad m^{-2}, depending also on the set of frequencies used in the analysis. Significantly larger positive values, between approximately 2000 and 10,000 rad m^{-2}, are

reported by Stirling et al. (2003) and Jorstad et al. (2007). However, RM values for the jet appear very stable, with smaller values in the range between -300 and ~ 150 rad m^{-2} (Zavala & Taylor 2003; O'Sullivan & Gabuzda 2009; Hovatta et al. 2012).

In Section 2, we present the observations and the specific details for the analysis of the space VLBI *RadioAstron* data. In Section 3, we present and analyze the *RadioAstron* image at 22 GHz, whose polarization is analyzed in more detail in Section 4. Finally, our conclusions and summary are presented in Section 5.

For a flat universe with $\Omega_m = 0.3$, $\Omega_\Lambda = 0.7$, and $H_0 = 70$ km s^{-1} Mpc^{-1} (Planck Collaboration et al. 2014), 1 mas corresponds to 1.295 pc at the redshift of BL Lac ($z = 0.0686$), and a proper motion of 1 mas yr^{-1} is equivalent to 4.51 c.

2. OBSERVATIONS AND DATA REDUCTION

2.1. RadioAstron *Space VLBI Observations at 22 GHz*

RadioAstron observations of BL Lac at 22.2 GHz (K band) were performed on 2013 November 10–11 (from 21:30 to 13:00 UT). A total of 26 ground antennas were initially scheduled for the observations, but different technical problems at the sites limited the final number of correlated ground antennas to 15, namely Effelsberg (EF), Metsaehovi (MH), Onsala (ON), Svetloe (SV), Zelenchukskaya (ZC), Medicina (MC), Badary (BD), and VLBA antennas Brewster (BR), Hancock (HN), Kitt Peak (KP), Los Alamos (LA), North Liberty (NL), Owens Valley (OV), Pie Town (PT), and Mauna Kea (MK).

The data were recorded in two polarizations (left and right circularly polarized, LCP and RCP), with a total bandwidth of 32 MHz per polarization, split into two intermediate frequency (IF) bands of 16 MHz. The SRT data were recorded by the *RadioAstron* satellite tracking stations (Kardashev et al. 2013; Ford et al. 2014) in Puschino (21:30 – 06:10 UT) and Green Bank (07:30 – 13:00 UT), including some extended gaps required for cooling of the motor drive of the on board high-gain antenna of the *Spektr-R* satellite. These gaps were used for the ground-only observations of BL Lac at 15 and 43 GHz (see Section 2.2), as well as observations of several calibrator sources.

Correlation of the data was performed using the upgraded version of the DiFX correlator developed at the Max-Planck-Institut für Radiostronomie (MPIfR) in Bonn (Bruni et al. 2014), enabling accurate calibration of the instrumental polarization of the SRT (see also Lobanov et al. 2015 for a more detailed description of the imaging and correlation of *RadioAstron* observations).

The correlated data were reduced and imaged using a combination of the AIPS and *Difmap* (Shepherd 1997) software packages. The a priori amplitude calibration was applied using the measured system temperatures for the ground antennas and the SRT. Sensitivity parameters of the SRT (Kovalev et al. 2014) are measured regularly during maintenance sessions. Parallactic angle corrections were applied to the ground antennas to correct for the feed rotation.

2.1.1. Fringe Fitting

Fringe fitting of the data was performed by first manually solving for the instrumental phase offsets and single band
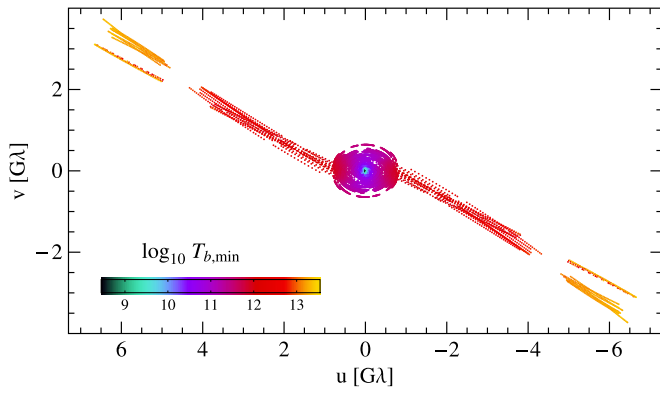
Figure 1. Fourier coverage (*uv*-coverage) of the fringe-fitted data (i.e., reliable fringe detections) of the *RadioAstron* observations of BL Lac on 2013 November 10–11 at 22 GHz. Color marks the lower limit of observed brightness temperature obtained from visibility amplitudes (for details, see the discussion in Section 3.3).

delays using a short scan during the perigee of the SRT, when the shortest projected ground–space baseline distances (smaller than one Earth diameter) are obtained, providing the best fringe solutions for the space antenna. These solutions were applied before performing a global fringe search for the delays and rates of the ground array only.

Once the ground antennas were fully calibrated, they were coherently combined to improve the fringe detection sensitivity of the SRT (Kogan 1996). This baseline stacking was carried out setting DPARM(1) = 3 in AIPS's FRING task, also performing an exhaustive baseline search and combining both polarizations and IFs to improve the sensitivity. Progressively longer solution intervals were used for the fringe search, from one minute to maintain the coherence of the signal during the acceleration of the spacecraft in the perigee to four minutes to increase the sensitivity on the longer baselines to the SRT.

The phasing of a group of ground-based antennas allowed us to obtain reliable ground-space fringe detections up to projected baselines of 7.9 Earth diameters (D_E) in length, covering the duration of the experiment within which Puschino was used as the tracking station. No further fringes were obtained to the spacecraft once the tracking station changed to Green Bank, which is presumably due to a difference in clock setting between the two tracking stations. These were searched for by introducing trial clock offsets for the Green Bank tracking station, and performing new test correlations with a larger fringe-search window of up to 1024 channels and 0.1 s of integration time in width. However, no further fringes were detected to the SRT. We also note that 1.5 hr passed between the last Puschino scan and the first Green Bank scan, thus increasing the space baseline length and perhaps reducing the correlated flux density below the sensitivity threshold. The resulting fringe-fitted data visibility coverage of the Fourier domain (*uv*-coverage) is shown in Figure 1.

After the fringe fitting the delay difference between the two polarizations was corrected using AIPS's task RLDLY, and a complex bandpass function was solved for the receiver.

2.1.2. Polarization Calibration

The instrumental polarization (D-terms) was obtained using AIPS's task LPCAL (Leppanen et al. 1995). Table 1 lists the instrumental polarization derived for each telescope, with Effelsberg as the reference antenna. Errors in the instrumental

Table 1
Instrumental Polarization (D-Terms) at 22 GHz

Antenna	RCP		LCP	
	m (%)	χ (°)	m (%)	χ (°)
SRT	9.3 ± 0.5	21 ± 5	4.5 ± 0.3	72 ± 5
	8.8 ± 0.8	20 ± 4	4.4 ± 0.2	68 ± 8
BR	1.4 ± 0.7	−73 ± 18	0.8 ± 0.4	−165 ± 22
	1.4 ± 0.7	−86 ± 23	0.7 ± 0.3	−196 ± 24
EF	9.9 ± 0.7	−91 ± 4	8.1 ± 0.5	−126 ± 7
	9.3 ± 0.8	−98 ± 3	7.5 ± 0.3	−130 ± 6
HN	2.3 ± 0.2	174 ± 16	2.2 ± 0.6	90 ± 6
	2.2 ± 0.4	149 ± 14	2.0 ± 0.8	85 ± 11
KP	1.1 ± 0.3	−160 ± 8	1.1 ± 0.4	−167 ± 12
	0.9 ± 0.4	−182 ± 5	1.0 ± 0.3	−194 ± 8
LA	2.4 ± 0.6	−62 ± 7	1.0 ± 0.4	−124 ± 8
	2.7 ± 0.7	−75 ± 6	0.8 ± 0.6	−126 ± 11
NL	3.6 ± 0.5	−43 ± 5	3.8 ± 0.2	−106 ± 9
	3.1 ± 0.6	−43 ± 7	4.0 ± 0.4	−104 ± 8
OV	2.0 ± 0.8	118 ± 8	2.3 ± 0.4	18 ± 7
	2.2 ± 0.8	94 ± 6	2.7 ± 0.4	13 ± 11
PT	1.4 ± 0.3	−85 ± 11	2.0 ± 0.5	−74 ± 9
	1.4 ± 0.4	−77 ± 12	2.0 ± 0.6	−65 ± 12
MH	1.9 ± 0.9	−116 ± 8	8.2 ± 1.3	−41 ± 9
	2.9 ± 0.8	−152 ± 6	5.5 ± 0.9	−57 ± 8
ON	4.1 ± 0.8	−43 ± 4	5.3 ± 0.5	−87 ± 7
	4.2 ± 0.9	−38 ± 8	5.2 ± 0.6	−82 ± 12
SV	4.8 ± 0.3	179 ± 7	4.1 ± 0.5	−2 ± 5
	4.7 ± 0.2	178 ± 10	4.0 ± 0.3	0 ± 4
ZC	6.1 ± 0.7	162 ± 13	8.3 ± 0.8	168 ± 9
	8.3 ± 0.6	111 ± 10	6.9 ± 0.9	165 ± 5
MC	0.9 ± 0.7	109 ± 10	6.1 ± 0.6	41 ± 8
	2.6 ± 0.9	87 ± 11	5.5 ± 0.9	42 ± 11
MK	3.3 ± 0.4	−64 ± 8	2.9 ± 0.3	−135 ± 5
	3.5 ± 0.6	−67 ± 12	2.9 ± 0.5	−130 ± 9
BD	7.7 ± 0.8	−99 ± 7	6.4 ± 0.6	−179 ± 6
	8.1 ± 0.9	−103 ± 8	6.7 ± 0.8	−178 ± 9

Note. Listed values correspond to the fractional amplitude, m, and phase, χ, of the instrumental polarization for each antenna and polarization in the first (top row) and second (bottom row) IF.

polarization were estimated from the dispersion in the values obtained by performing independent data reductions while using different reference antennas, as well as comparison with values obtained for calibrator sources (2021+614 and 1823+568). Estimated values for the ground antennas are also subject to antenna performance and weather conditions at the sites, which in some cases may lead to larger than usual instrumental polarization values. Amplitude and phase stability across the two IFs confirms the reliability of the estimated values.

Instrumental polarization of the SRT at 22 GHz is less than 9% (5% for LCP), and remarkably consistent across the two
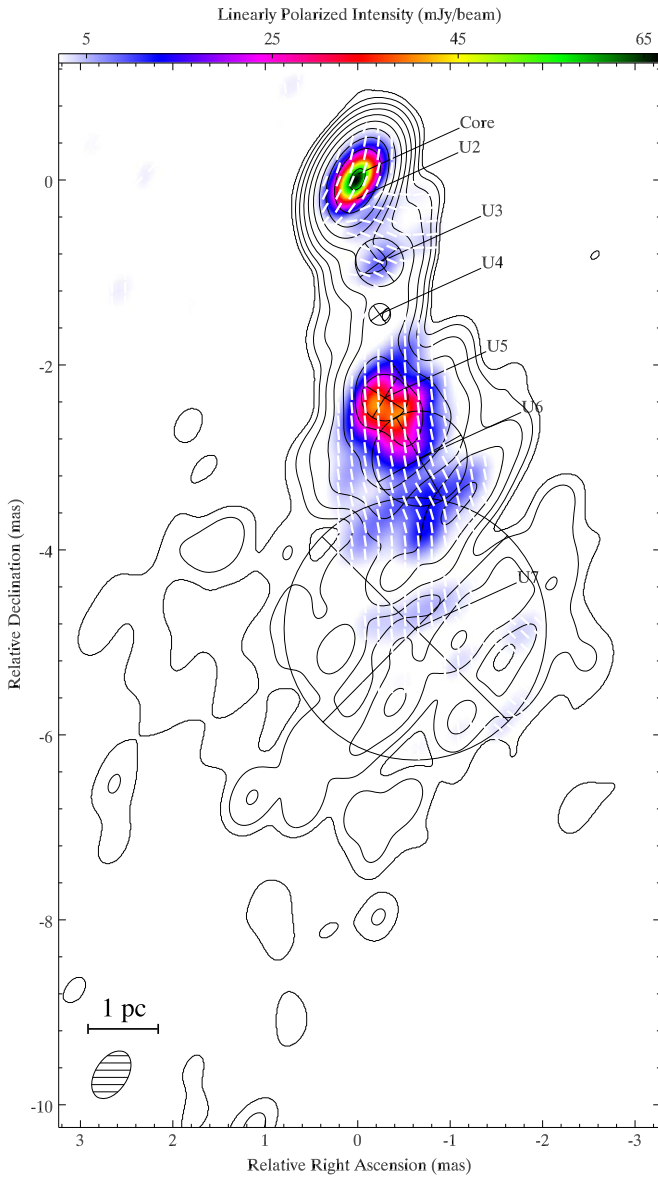
Figure 2. Ground-array 15 GHz observations of BL Lac on 2013 November 10. Total intensity contours are plotted at 0.05%, 0.11%, 0.24%, 0.57%, 1.32%, 3.08%, 7.16%, 16.64%, 38.70%, and 90% of the peak intensity at 3.31 Jy/beam. Linearly polarized intensity is shown in colors starting at 2 mJy/beam, and bars indicate the EVPA. Synthesized beam FWHM is 0.57×0.35 mas at a position angle of $-33°$. Model fit components are also shown overlaid, indicating their position and angular size (see also Table 2).

Figure 3. VLBA-BU-BLAZAR image of BL Lac at 43 GHz obtained in 2013 November 18. Total intensity contours are plotted at 0.25%, 0.48%, 0.92%, 1.78%, 3.42%, 6.57%, 12.65%, 24.33%, 46.79%, and 90% of the peak at 2.7 Jy/beam. Linearly polarized intensity is shown in colors starting at 6.8 mJy/beam, and bars indicate the EVPA. Synthesized beam FWHM is 0.25×0.16 mas at a position angle of $-5°$. Model fit components are also shown overlaid, indicating their position and angular size (see also Table 2).

IFs, demonstrating its robust polarization capabilities for *RadioAstron* imaging observations at its highest observing frequency of 22 GHz.

Absolute calibration of the electric vector position angle (EVPA) was obtained from comparison with simultaneous single dish observations at the Effelsberg telescope of our target and calibrator sources. We estimate the error in the EVPA calibration to lie between 5° and 10°.

2.2. Ground-array Observations at 15 and 43 GHz

Simultaneous ground-only observations of BL Lac at 15.4 and 43.1 GHz were obtained during gaps in the *RadioAstron*
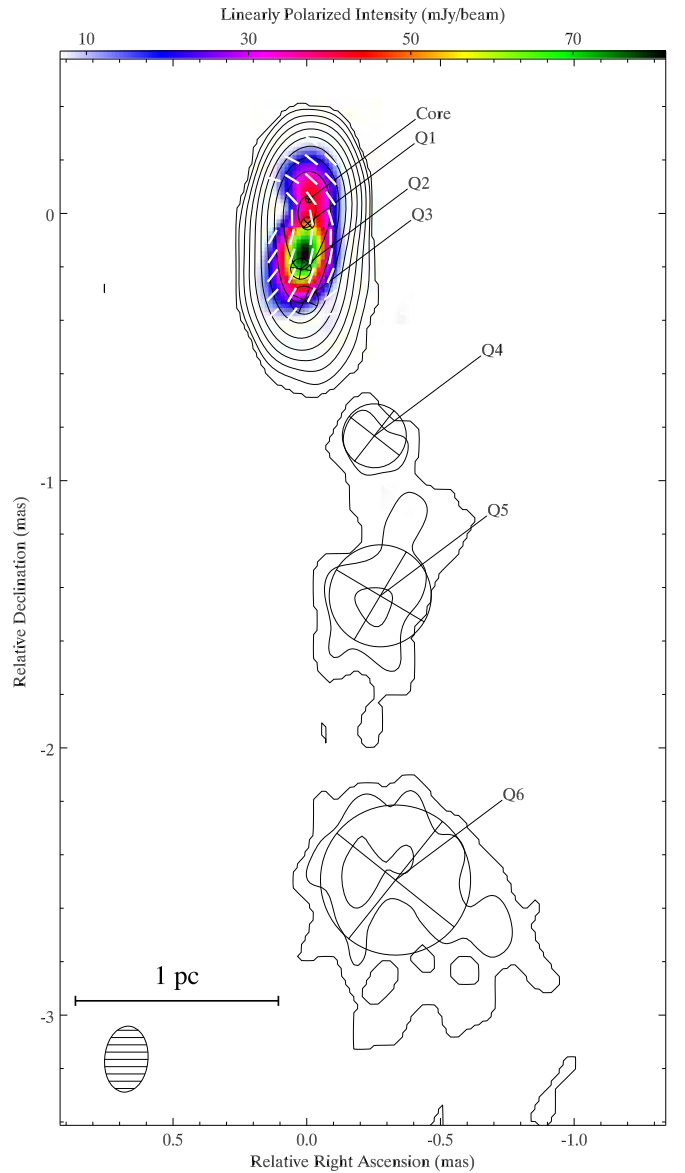
observations. Participating antennas were Effelsberg and VLBA antennas BR, HN, KP, LA, NL, OV, and PT. However, at 43 GHz, no fringes were detected on the intercontinental baselines with Effelsberg due to technical problems severely limiting the sensitivity and angular resolution, and in fact preventing the detection of polarization at this frequency. For this reason, we have used instead the 43 GHz data from the VLBA-BU-BLAZAR[11] monitoring program, performed on 2013 November 18, only one week after our observations.

Calibration of the 15 GHz data follows that outlined previously in Section 2.1, except for the particular steps related more directly to the space VLBI observations, such as the
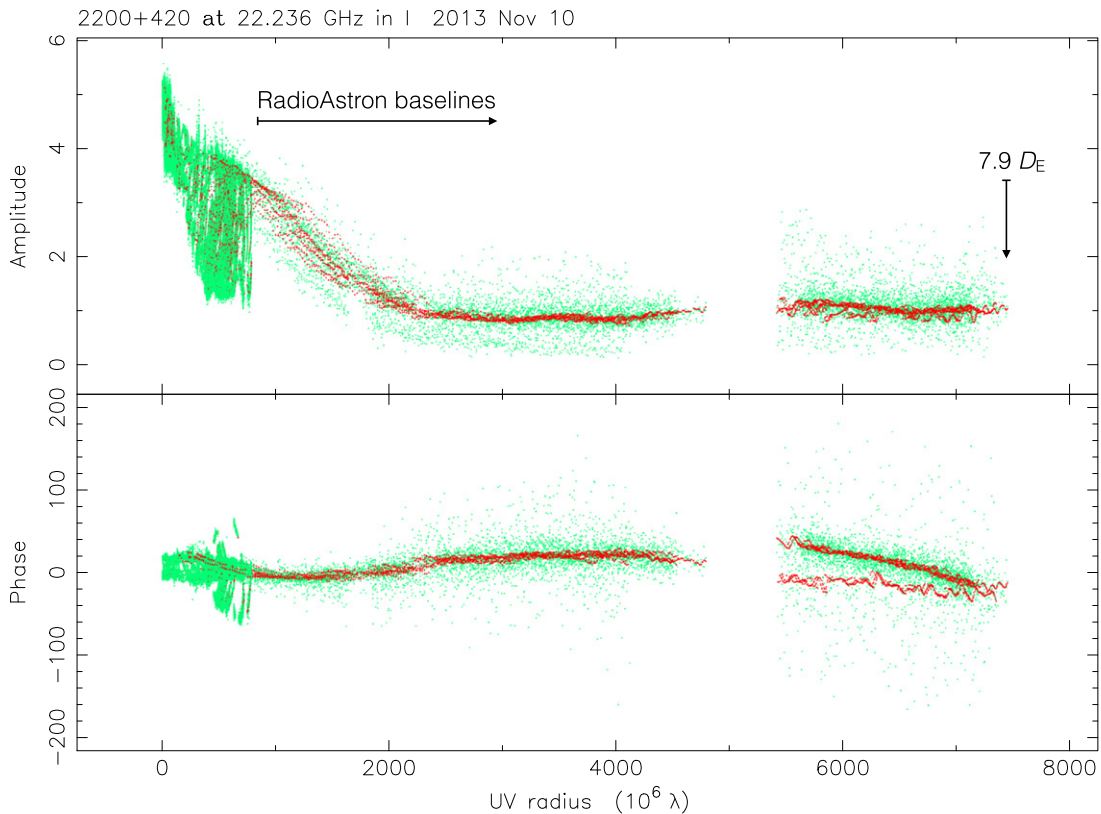
---

[11] see https://www.bu.edu/blazars/VLBAproject.html

Figure 4. Self-calibrated visibility amplitudes and phases as a function of *uv*-distance of the *RadioAstron* observations of BL Lac on 2013 November 10–11 at 22 GHz. Overplotted in red is the fit to these data of the CLEAN model obtained from the hybrid mapping. Reliable space–ground fringe detections were obtained up to a projected baseline length of 7.9 Earth diameters.

phasing of the ground array during the fringe fitting. Calibration of the absolute orientation of the EVPAs was also performed by comparison with Effelsberg single dish observations of BL Lac ($S_{15\,GHz} = 5.57 \pm 0.23$ Jy, $m = 3.44 \pm 0.3\%$, EVPA $= 3°.7 \pm 1°.1$), with an estimated error of 5°–7°.

Figures 2 and 3 show the 15 and 43 GHz images of BL Lac obtained with the ground array. To characterize the emission structure, we have performed a fit of the complex visibilities by a set of components with circular Gaussian brightness distributions, listed in Table 2.

3. SPACE VLBI POLARIMETRIC IMAGES OF BL LAC AT 21 μAS ANGULAR RESOLUTION

Fully calibrated *RadioAstron* data were exported to *Difmap* and imaged using the standard hybrid imaging and self-calibration techniques. Self-calibrated Stokes I visibility amplitudes and phases as a function of Fourier spacing (*uv* distance) and CLEAN model fit to these data are shown in Figure 4. Space VLBI fringes to the SRT extend the projected baseline spacing up to 7.9 D_E, increasing accordingly the angular resolution with respect to that provided by ground-based arrays. However, the large eccentricity of the SRT orbit (see Figure 1) leads to a highly elliptical observing beam.

RadioAstron space VLBI polarimetric images of BL Lac are shown in Figure 5 for three different visibility weights: natural, uniform, and "super" uniform (in which the gridding weights are not scaled by the visibility amplitude errors). The weights of the longest space VLBI visibilities are therefore increasingly higher from natural to super uniform weightings, consequently yielding higher angular resolutions, albeit with lower image

sensitivities. The super uniform weighting image yields an angular resolution of 21 μas (along the minor axis of the restoring beam), which to our knowledge corresponds to the *highest achieved to date*. For an estimated black hole mass of $\sim 1.6 \times 10^8\ M_\odot$ (Woo & Urry 2002), where $M_\odot$ is the mass of the Sun, this corresponds to a linear resolution of ~ 1800 Schwarzschild radii at the BL Lac distance.

The images in Figure 5 show the familiar radio continuum emission structure of BL Lac, dominated by the core and a jet that extends to the south. Conveniently, the highest angular resolution provided by the ground–space baselines is obtained nearly along the jet direction, allowing close examination of the innermost structure of the jet. As can be better distinguished in the uniform (Figure 5b) and super uniform (Figure 5c) images, the total intensity images reveal a bent structure in the innermost 0.5 mas region. The linearly polarized images clearly distinguish two components in this region, as well as in the jet area at ~ 3 mas from the core.

3.1. Stationary Components in the Innermost 0.5 mas Region

Previous high angular resolution monitoring programs of BL Lac systematically show the presence of two stationary features close to the core (Stirling et al. 2003; Jorstad et al. 2005; Mutel & Denn 2005). In particular, Jorstad et al. (2005) report, through an analysis of a sequence of 17 bimonthly VLBA observations at 43 GHz, two stationary components, labeled A1 and A2, located at a mean distance from the core (position angle) of 0.10 and 0.29 mas ($-160°$ and $-159°$), respectively. These can be associated with components
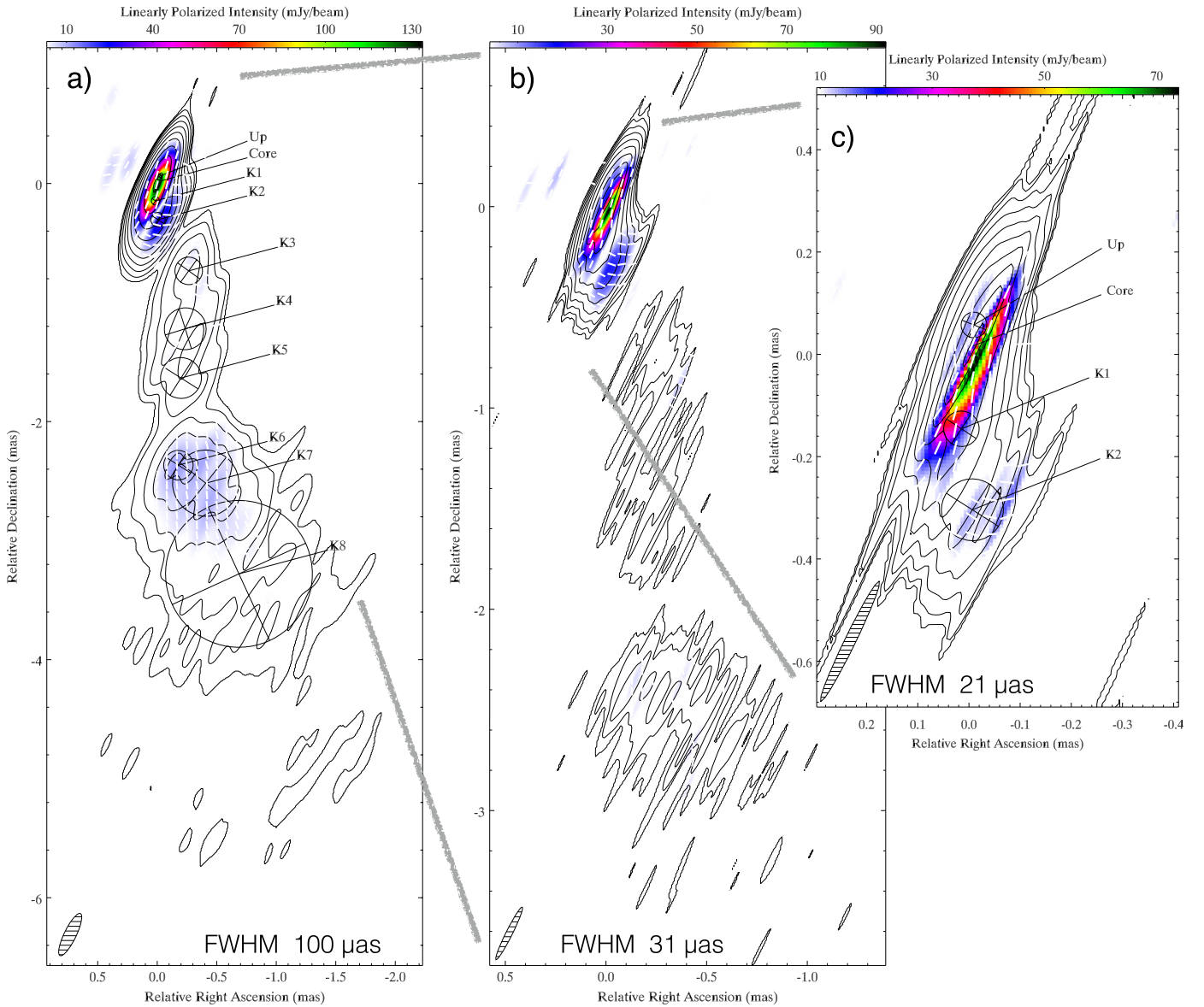
Figure 5. *RadioAstron* polarimetric space VLBI images of BL Lac obtained in 2013 November 10–11 at 22 GHz. From left to right, images are obtained with natural (a), uniform (b), and "super"-uniform (c) weightings. Total intensity contours are plotted at 0.08%, 0.17%, 0.36%, 0.80%, 1.76%, 3.86%, 8.49%, 18.65%, 40.97%, and 90% (0.2%, 0.4%, 0.78%, 1.54%, 3.04%, 5.99%, 11.79%, 23.22%, 45%, 71%, and 90%; 0.76%, 1.3%, 2.21%, 3.75%, 6.37%, 10.81%, 18.37%, 31.2%, 23%, and 90%) of the peak intensity at 2.48 (1.48; 1.23) Jy/beam for the natural weighted image (uniform; "super"-uniform). Linearly polarized intensity is shown in colors starting at (a) 3.1 mJy/beam, (b) 3.8 mJy/beam, and (c) 9.4 mJy/beam, and white bars indicate the (*uncorrected* for Faraday rotation) EVPAs. Synthesized beams are (a) 0.392×0.100 mas, (b) 0.292×0.031 mas, and (c) 0.261×0.021 mas at a common position angle of $-26°$.

C2 and C3 in Mutel & Denn (2005), respectively, obtained from independent 43 GHz VLBA observations.

More recently, Cohen et al. (2014, 2015) present an analysis of more than a decade of 15 GHz VLBA observations of BL Lac from the MOJAVE monitoring program. These observations confirm the existence of a stationary component, labeled C7 by these authors, located at a mean distance from the core of 0.26 mas and at a position angle of $-166°.6$, in agreement with component A2 reported by Jorstad et al. (2005).

This is also corroborated by our 15 and 43 GHz observations (see Table 2 and Figures 2 and 3), in which components U2 and Q2 would correspond to previously identified components A2 and C7, and component Q1 to A1.

Our measured position angles for the two stationary features (Q1 and Q2/U2) are slightly offset to the east by $\sim 20°$ with respect to the main values published by Jorstad et al. (2005) and Cohen et al. (2014). This may be associated with the jet precession reported by Stirling et al. (2003) and Mutel & Denn (2005), leading to a swing in the position angle of the innermost components. A similar variation in the position angle of component U2 is seen in MOJAVE observations by Cohen et al. (2014).

3.2. Evidence for Emission Upstream of the Core

Model fitting of the innermost structure in our *RadioAstron* observations, listed in Table 2 and plotted in Figure 5, shows two close components near the core region, as well as two other

Table 2
Gaussian Model Fits for the 22 GHz *RadioAstron* and Ground-array Data at 43 and 15 GHz

Comp.	Flux (mJy)	Distance (mas)	PA (°)	Size (mas)	T_b (K)	m (%)	EVPA (°)
RadioAstron 22 GHz							
Up	1578 ± 72	0.041 ± 0.003	-1 ± 4	0.050 ± 0.003	$(1.56 \pm 0.26) \times 10^{12}$	4.0 ± 0.4	17 ± 1
Core	802 ± 43	...	...	<0.01	$>2.0 \times 10^{13}$	4.8 ± 0.4	16 ± 1
K1	1128 ± 37	0.164 ± 0.004	172 ± 1	0.067 ± 0.003	$(5.82 \pm 0.70) \times 10^{11}$	5.7 ± 0.5	17 ± 1
K2	578 ± 12	0.320 ± 0.008	179 ± 1	0.122 ± 0.004	$(9.79 \pm 0.85) \times 10^{10}$	8.6 ± 2.0	84 ± 5
K3	79 ± 12	0.79 ± 0.03	-161 ± 2	0.231 ± 0.012	$(3.64 \pm 0.93) \times 10^{9}$	...	...
K4	111 ± 13	1.26 ± 0.04	-170 ± 1	0.352 ± 0.018	$(2.22 \pm 0.49) \times 10^{9}$	...	...
K5	70 ± 13	1.66 ± 0.05	-173 ± 2	0.343 ± 0.017	$(1.47 \pm 0.42) \times 10^{9}$	...	...
K6	108 ± 12	2.39 ± 0.02	-176 ± 1	0.247 ± 0.012	$(4.39 \pm 0.91) \times 10^{9}$	20.8 ± 2.4	4 ± 4
K7	283 ± 14	2.57 ± 0.04	-171 ± 1	0.556 ± 0.056	$(2.26 \pm 0.57) \times 10^{9}$	26.2 ± 6.7	8 ± 3
K8	214 ± 15	3.37 ± 0.11	-168 ± 2	1.23 ± 0.12	$(3.48 \pm 0.92) \times 10^{8}$	...	...
VLBA-BU-BLAZAR Ground-array Data at 43 GHz							
Core	1575 ± 72	...	...	0.026 ± 0.005	$(1.48 \pm 0.63) \times 10^{12}$	1.7 ± 0.2	37 ± 6
Q1	1373 ± 65	0.091 ± 0.005	177 ± 8	0.048 ± 0.005	$(3.92 \pm 1.00) \times 10^{11}$	2.0 ± 0.3	7 ± 4
Q2	786 ± 32	0.262 ± 0.005	173 ± 1	0.077 ± 0.007	$(8.68 \pm 1.93) \times 10^{10}$	5.4 ± 0.1	18 ± 2
Q3	402 ± 18	0.378 ± 0.008	177 ± 1	0.105 ± 0.009	$(2.40 \pm 0.52) \times 10^{10}$	3.1 ± 0.8	29 ± 4
Q4	50 ± 10	0.92 ± 0.07	-165 ± 5	0.239 ± 0.012	$(5.79 \pm 1.74) \times 10^{8}$	...	...
Q5	100 ± 11	1.51 ± 0.08	-170 ± 3	0.382 ± 0.019	$(4.52 \pm 0.95) \times 10^{8}$	...	...
Q6	209 ± 13	2.57 ± 0.09	-173 ± 2	0.562 ± 0.028	$(4.34 \pm 0.70) \times 10^{8}$	...	...
Ground-array Data at 15 GHz							
Core	2705 ± 124	...	...	<0.06	$>7.9 \times 10^{12}$	2.0 ± 0.1	20 ± 1
U2	1193 ± 60	0.266 ± 0.019	-177 ± 5	<0.06	$>3.5 \times 10^{12}$	1.5 ± 0.1	30 ± 1
U3	266 ± 23	0.982 ± 0.025	-166 ± 2	0.523 ± 0.026	$(5.03 \pm 0.94) \times 10^{9}$	5.5 ± 1.7	67 ± 3
U4	84 ± 13	1.53 ± 0.02	-171 ± 1	0.235 ± 0.012	$(7.87 \pm 2.00) \times 10^{9}$	...	...
U5	462 ± 32	2.43 ± 0.02	-173 ± 1	0.503 ± 0.025	$(9.44 \pm 1.59) \times 10^{9}$	18.9 ± 4.0	5 ± 1
U6	332 ± 27	3.15 ± 0.04	-167 ± 1	1.03 ± 0.05	$(1.62 \pm 0.29) \times 10^{9}$	27.0 ± 18	16 ± 8
U7	391 ± 33	4.96 ± 0.12	-173 ± 2	2.84 ± 0.14	$(2.52 \pm 0.46) \times 10^{8}$	...	...

Note. Tabulated data correspond to component's label, flux density, distance and position angle from the core, size, observed brightness temperature, degree of linear polarization, and electric vector position angle, *uncorrected* for Faraday rotation (see Section 4).

components within the innermost 0.5 mas region. The fitted circular Gaussian components provide an accurate representation of the jet emission, yielding a residual map (uniform weighting) with an rms of 1.4 mJy/beam and minimum and maximum residuals of -45 mJy/beam and 53 mJy/beam, respectively. Allowing for elliptical Gaussian components provides very similar fitted values as those listed in Table 2 with no significant improvement in the residuals.

We can tentatively identify components K1 and K2 with the previously discussed stationary features Q1 and Q2 (U2). However, identification of the two-component structure in the core area requires a more detailed analysis of the evolution of the innermost structure of the jet.

For this, we have performed model fitting of the 43 GHz VLBA images from the VLBA-BU-BLAZAR program extending our analysis to cover the period between 2013 December and 2014 June, comprising a total of five more epochs with a cadence of roughly one month. The obtained model fits are listed in Table 3, and Figure 7 plots the component's distance from the core versus time. Stationary components Q1 and Q2 are detected at all epochs. Analysis of their flux densities show that Q1 becomes unusually bright (2.1 Jy) on 2013 December 16, followed by a similar increase in flux density of Q2 (1.1 Jy) on 2014 January 19. This could be associated with the passing of a new component, M1, through the standing features, leading to a brief increase in their

flux densities (e.g., Gómez et al. 1997). Component M1 is identified in the last two epochs as a weak knot beyond 0.5 mas from the core. The estimated apparent speed for this new component is 7.9 ± 0.3 c (1.76 ± 0.06 mas yr^{-1}), in agreement with values previously found in BL Lac (Jorstad et al. 2005), giving an ejection date of 2013.89 ± 0.05, or 2013 November 23 (±18 days), in coincidence with our *RadioAstron* observations within the errors.

Considering the measured proper motion of the new component and the estimated time of crossing through the 43 GHz core, we can estimate that component M1 should be placed ~50 μas *upstream* of the core in our *RadioAstron* image, or slightly smaller if we allow for some initial acceleration. Based on this, we consider that the core of the jet in our *RadioAstron* observations corresponds to the unresolved component labeled "Core," upstream of which component "Up" would correspond to component M1 identified also at 43 GHz. Evidence for emission upstream of the core is also found by looking at the 43 GHz polarization image (see Figure 3), which shows polarized emission to the north with a different orientation of the polarization vectors than the remaining core area.

We note that the appearance of new superluminal components *upstream* of the core in BL Lac has been previously reported by Marscher et al. (2008), associated with a multiwavelength outburst. Similarly, the radio, optical, and
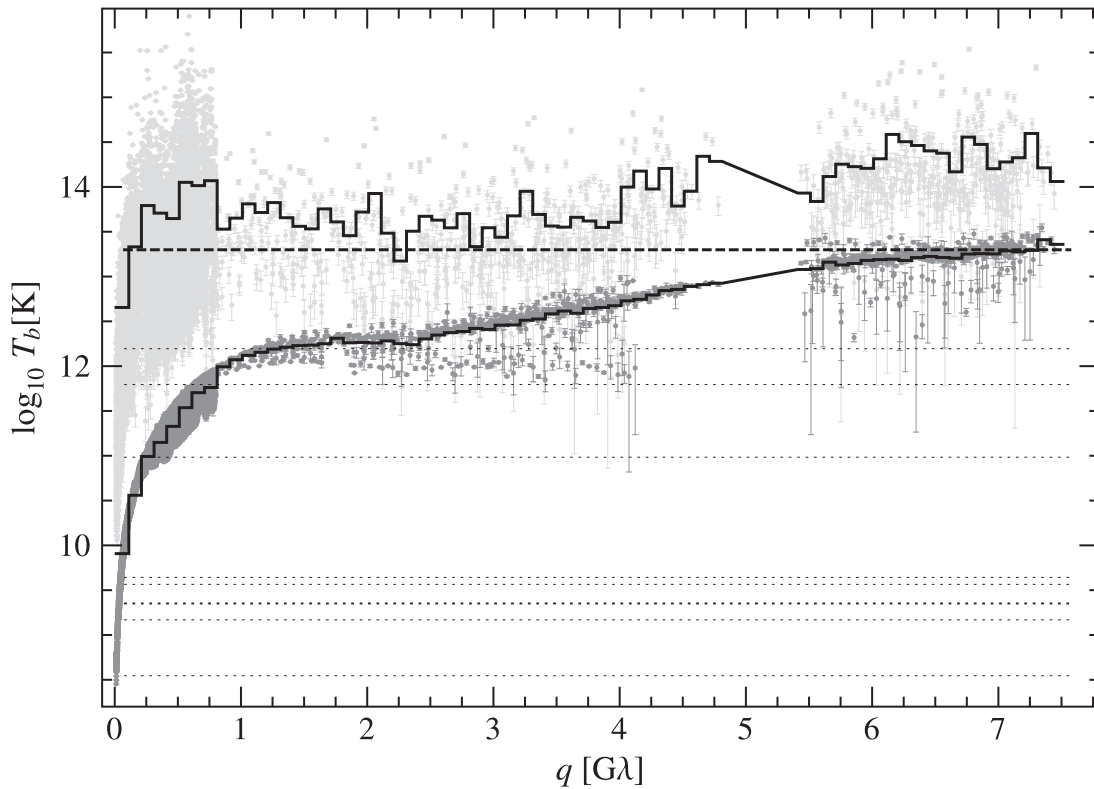
Figure 6. Visibility-based estimates of the observed brightness temperature in BL Lac, calculated from the *RadioAstron* data at 22 GHz. Data points represent the minimum (dark gray), $T_{b,min}$, and maximum (light gray), $T_{b,max}$, brightness temperatures derived from individual visibilities measured at different *uv* distances, q (Lobanov 2015). The two-dimensional distribution of $T_{b,min}$ is also presented in Figure 1 with a color wedge. The histograms show the respective brightness temperatures averaged over bins of 0.1 Gλ in size. The thick dashed line indicates the lower limit on brightness temperature, $T_{b,mod} > 2 \times 10^{13}$ K, derived for the core component of the source structure described in Table 2. The dotted lines indicate the respective brightness temperatures of the rest of the model components. The minimum brightness temperature, $T_{b,min} = 1.5 \times 10^{13}$ K, is constrained by the visibilities with $q > 5.3$ Gλ. The estimated maximum brightness temperature $T_{b,max} = 3.1 \times 10^{14}$ K is calculated from the data on the same baselines.

γ-ray light curves (see the VLBA-BU-BLAZAR web page[12]) show a flare at the end of 2013, close in time to our *RadioAstron* observations.

3.3. Brightness Temperature

Table 2 also lists the observed (i.e., not corrected for redshift or Doppler boosting) brightness temperatures, estimated from the model-fitted circular Gaussian components as $T_b = 1.36 \times 10^9 S \lambda^2/\theta^2$ [K], where S (in Jansky) is the total flux density, θ (mas) is the size, and λ (cm) is the observing wavelength (e.g., Kovalev et al. 2005). Model-fitted data of the *RadioAstron* visibilities yield a brightness temperature of $(1.56 \pm 0.26) \times 10^{12}$ K for the component upstream of the core, "Up," while for the unresolved core component, "Core," we obtain a lower limit of $T_b > 2.0 \times 10^{13}$ K.

The observed brightness temperature in jets is mostly affected by the transverse dimension of the flow and it may differ systematically from estimates obtained on the basis of representing the jet structure with Gaussian components (Lobanov 2015). In this case, constraints on the jet brightness temperature can also be found directly from visibility amplitudes and their errors, providing the minimum brightness temperature, $T_{b,min}$, and an estimate of the formal maximum brightness temperature, $T_{b,max}$ that can be obtained under the

condition that the structural detail sampled by the given visibility is resolved. For further details, we refer the reader to Lobanov (2015).

These two estimates are compared in Figure 6 with the brightness temperatures calculated from the Gaussian components described in Table 2. One can see that the observed brightness temperature of the most compact structures in BL Lac, constrained by baselines longer than 5.3 Gλ, must indeed exceed 2×10^{13} K and can reach as high as $\sim 3 \times 10^{14}$ K. As follows from Figure 1, these visibilities correspond to the structural scales of 30–40 μas oriented along position angles of 25°–30°. These values are indeed close to the width of the inner jet and the normal to its direction.

The observed, $T_{b,obs}$, and intrinsic, $T_{b,int}$, brightness temperatures are related by

$$T_{b,obs} = \delta (1 + z)^{-1} T_{b,int}$$

where $\delta = (1 - \beta^2)^{1/2}(1 - \beta \cos \phi)^{-1}$ is the Doppler factor, β is the jet bulk velocity in units of the speed of light, ϕ is the jet viewing angle, and z is the redshift of the source. Variability arguments (Jorstad et al. 2005; Hovatta et al. 2009) and kinematical analyses (Cohen et al. 2015) yield a remarkably consistent value of $\delta = 7.2$, from which we estimate a lower limit of the intrinsic brightness temperature in the core component of our *RadioAstron* observations of $T_{b,int} > 2.9 \times 10^{12}$ K.

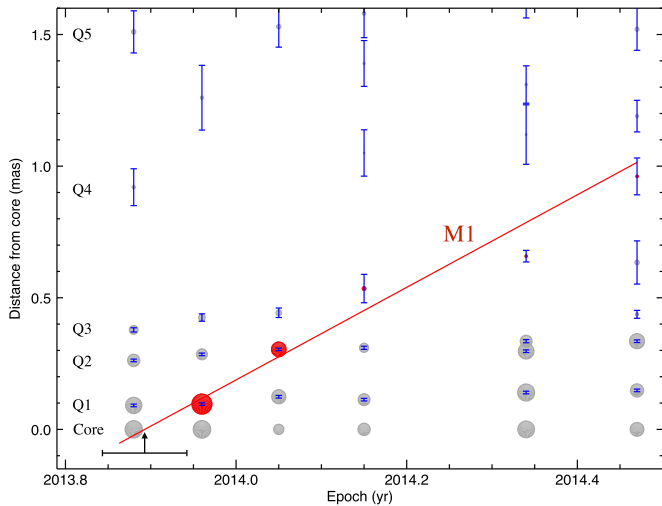[12] https://www.bu.edu/blazars/VLBA_GLAST/bllac.html

Figure 7. VLBA-BU-BLAZAR model fits covering 2013 November through 2014 June. Symbol size is proportional to the square root of the component's flux density. Marked in red is a new superluminal component, M1, with a proper motion of $7.9 \pm 0.3\ c$, ejected from the core in 2013.89 ± 0.05 (marked with an arrow and its respective error bar).

It is commonly considered that inverse Compton losses limit the intrinsic brightness temperature for incoherent synchrotron sources, such as AGNs, to about 10^{12} K (Kellermann & Pauliny-Toth 1969). In the case of a strong flare, the "Compton catastrophe" is calculated to take about one day to drive the brightness temperature below 10^{12} K. Moreover, Readhead (1994) has argued that, for sources near the equipartition of energy between the magnetic field and radiating particles, a more accurate upper value for the intrinsic brightness temperature is about 10^{11} K (see also Lähteenmäki et al. 1999; Hovatta et al. 2009), which is often called the equipartition brightness temperature.

Our estimated lower limit for the intrinsic brightness temperature of the core in the *RadioAstron* image of $T_{b,int} > 2.9 \times 10^{12}$ K is, therefore, more than an order of magnitude larger than the equipartition brightness temperature limit established by Readhead (1994), and at least several times larger than the limit established by inverse Compton cooling. This suggests that the jet in BL Lac is not in equipartition, as may be expected in the case in which the source is flaring during the ejection of component M1 detected at 43 GHz, and raises the possibility that we are significantly underestimating its Doppler factor.

We also note that if our estimate of the maximum brightness temperature is closer to actual values, it would imply $T_{b,int} \sim 5 \times 10^{13}$ K. This is difficult to reconcile with incoherent synchrotron emission models from relativistic electrons, requiring alternative models such as emission from relativistic protons (Jukes 1967), or coherent emission (Benford & Tzach 2000)—see also Kellermann (2002) and references therein.

4. POLARIZATION AND FARADAY ROTATION ANALYSIS

Our polarimetric observations with the ground arrays at 15 and 43 GHz and the space VLBI *RadioAstron* observations at 22 GHz can be combined to obtain an RM image of BL Lac.
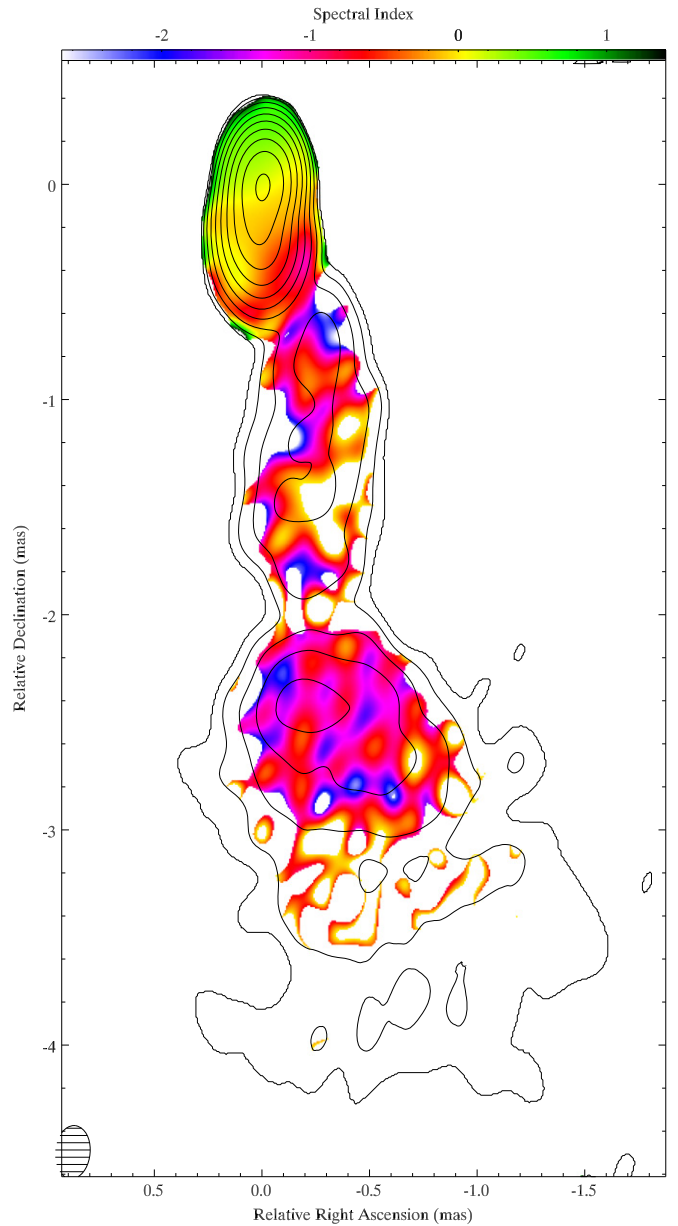

Figure 8. Spectral index image between the 22 GHz *RadioAstron* and 43 GHz ground-array total intensity images. Contours show the total intensity image from the *RadioAstron* observations convolved with the 43 GHz beam.

Data at 43 and 22 GHz were first tapered and convolved with a common restoring beam to match the 15 GHz resolution.

The combination of the images at all three frequencies also requires proper registration. Due to the difficulties in finding compact, optically thin components that could be matched across images, we have used for the image alignment a method based on a cross-correlation analysis of the total intensity images (Walker et al. 2000; Croke & Gabuzda 2008; Hovatta et al. 2012). Only optically thin regions have been considered in the cross-correlation analysis to avoid shifts in the core position due to opacity (e.g., Lobanov 1998; Kovalev et al. 2008) that could influence our results. We obtain a shift to the south, in the direction of the jet, of 0.021 mas and 0.063 mas for the alignment of the 22 and 15 GHz images, respectively, with respect to the one at 43 GHz.
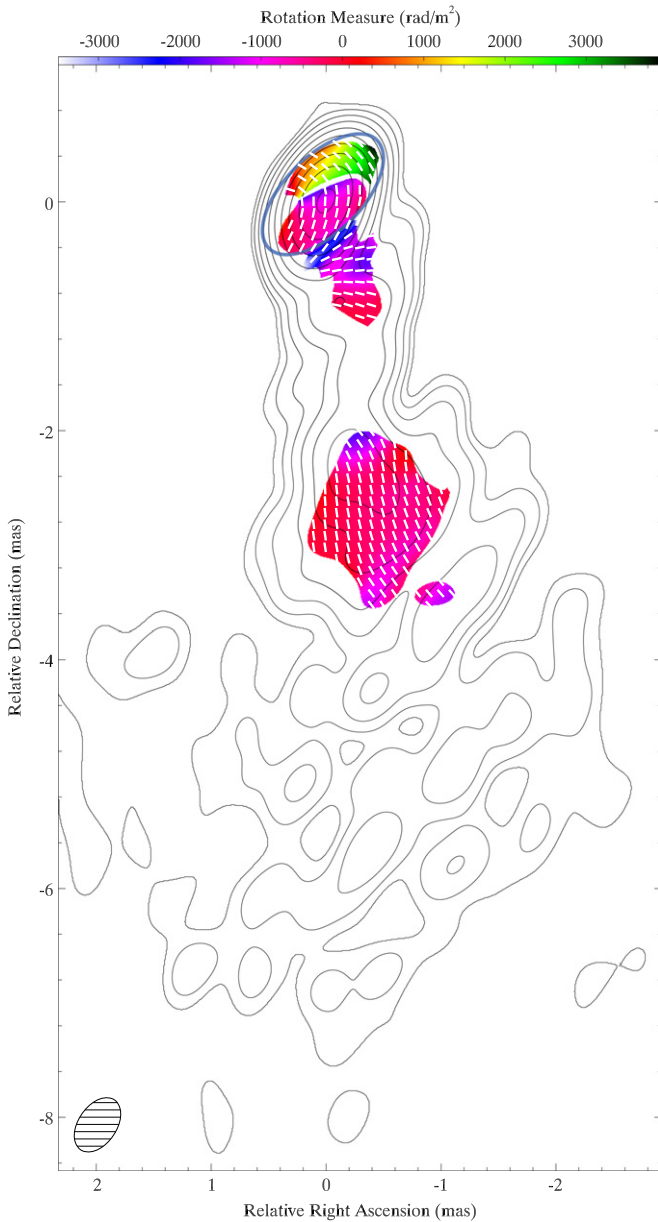
Figure 9. Rotation measure map combining the ground-array images at 15 and 43 GHz with the *RadioAstron* image at 22 GHz. Contours show the 15 GHz image, colors indicate the rotation measure, and bars plot the *Faraday-corrected* EVPAs. The light blue ellipse delimits the core region within which the 2D histogram images (see Figure 10) have been computed.

Figure 10. Probability density functions of the two-dimensional histograms of the rotation measure (a, top) and Faraday-corrected EVPA (b, bottom) for the core area indicated by the blue ellipse in Figure 9.

Pixels in the images for which polarization was not detected at all three frequencies simultaneously were blanked. The rotation measure (RM) map is computed by performing a λ^2 fit to the wavelength dependence of the EVPAs at each pixel, blanking pixels with a poor fit based on a χ^2 criterion. Due to the $n\pi$ ambiguity in the EVPAs, we have developed an IDL routine that searches for possible $n\pi$ rotations, finding that no wraps higher than $\pm\pi$ were required to fit the data.

When performing the RM analysis of the core area, it is also important to pay special attention to possible $\pi/2$ rotations due to opacity (e.g., Gómez et al. 1994; Gabuzda & Gómez 2001; Porth et al. 2011). We have checked for these by first computing the spectral index maps between each pair of frequencies. Figure 8 shows the spectral index map between the

22 GHz *RadioAstron* and 43 GHz VLBA images. This reveals an optically thick region at 22 GHz (and therefore also at 15 GHz) at the upstream end of the jet, near the core. This optically thick region is accounted for when computing the RM map by rotating the EVPAs at 22 and 15 GHz by $\pi/2$. The resulting RM map is shown in Figure 9.

4.1. Evidence for a Helical Magnetic Field

The RM and RM-corrected EVPAs (χ_0) in the core area (delimited by the blue ellipse in Figure 9) exhibit a clear point symmetry around its centroid. To better analyze this structure, Figure 10 displays the probability distribution function of the two-dimensional histogram for the RM and χ_0 as a function of the position angle of the pixels with respect to the centroid of the core, measured counterclockwise from north.

By inspecting Figures 9 and 10(a), we note a gradient in RM with position angle from the centroid of the core, with positive RM values in the area upstream of the centroid, and negative downstream, in the direction of the jet. The largest RM values, of the order of 3000 rad m^{-2}, are found in the area northeast of
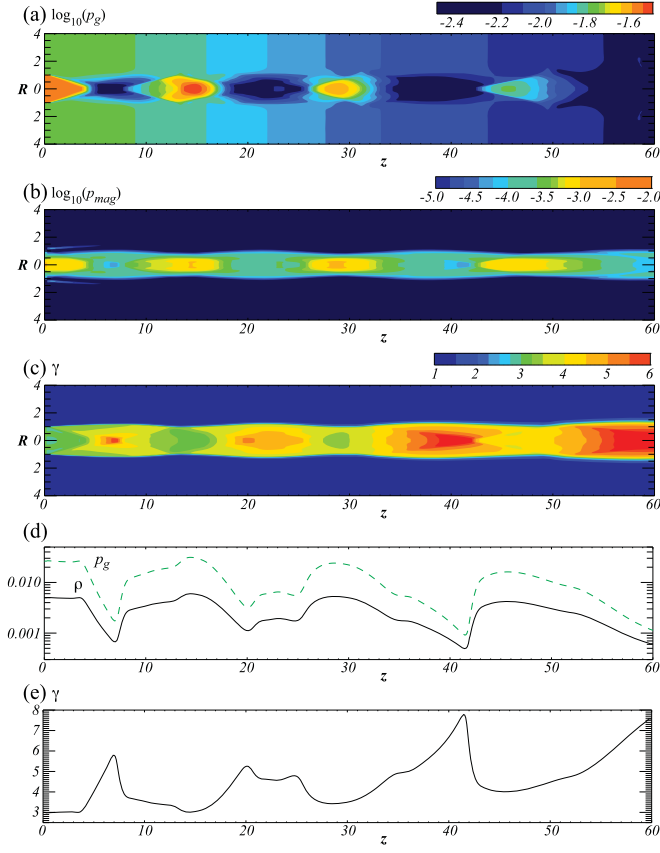
Figure 11. Relativistic magnetohydrodynamic simulations for an over-pressured jet propagating from left to right with a helical magnetic field at $t_s = 600$, where t_s is in units of R_j/c. Upper panels: 2D plots of (a) the gas pressure density, (b) the magnetic pressure ($p_{mag} = B^2/2$), and (c) the Lorentz factor. Lower panels: 1D profiles along the jet axis ($R = 0$) of (d) the rest-mass density (solid) and the gas pressure (green dashed), and (e) the Lorentz factor.

the centroid (with a position angle of approximately $-45°$); smaller values are obtained as the position angle increases, reaching values of ~ 1000 rad m^{-2} northwest of the centroid. Downstream of the centroid the RM continues this trend, reaching values of approximately -900 rad m^{-2} in the direction of the jet.

Similarly, Figures 9 and 10(b) show a progressive rotation in χ_0 with position angle from the centroid of the core. Counterclockwise from east, χ_0 rotate continuously from approximately $-25°$ to $\sim 60°$. On top of this, the two-dimensional histogram shows a concentration of χ_0 values between approximately $30°$ and $50°$ in the area upstream of the centroid, while downstream these concentrate in values at approximately $-25°$ and $0°$.

A similar dependence of the RM and χ_0 with polar angle was found by Zamaninasab et al. (2013) in 3C 454.3, interpreted by these authors as the result of a helical magnetic field. Indeed, gradients in RM across the jet width are expected to arise in the case of helical magnetic fields (Laing 1981), as previously reported in a number of sources (e.g., Asada et al 2002; O'Sullivan & Gabuzda 2009; Hovatta et al. 2012).

Relativistic magnetohydrodynamic (RMHD) simulations have been used to study the RM and polarization distribution based on self-consistent models for jet formation and propagation in the presence of large-scale helical magnetic fields (Broderick & McKinney 2010; Porth et al. 2011). These simulations reproduce the expected gradients in RM across the
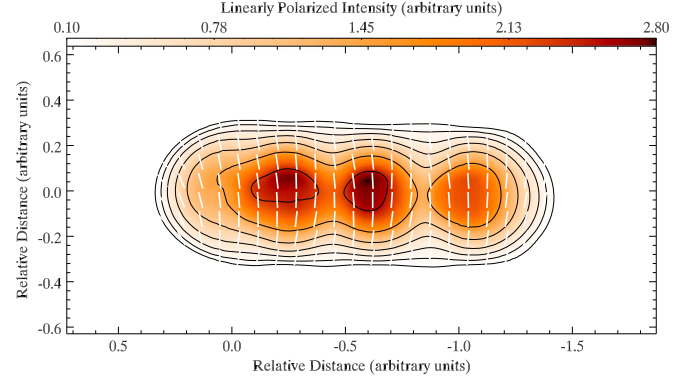

Figure 12. Simulated total intensity (contours, in logarithmic scale), linearly polarized intensity (colors), and EVPAs (bars) obtained by computing the (optically thin) radio continuum synchrotron emission at a viewing angle of $10°$ using the RMHD model shown in Figure 11 as input.

jet width due to the toroidal component of the helical magnetic field and also provide detailed insights regarding the polarization structure throughout the jet, which depends strongly on the helical magnetic field pitch angle, jet viewing angle, Lorentz factor, and opacity.

As discussed in Zamaninasab et al. (2013), Broderick & McKinney (2010), and Porth et al. (2011), a large-scale helical magnetic field would lead to similar point symmetric structures around the centroid of the core of both RM and χ_0 as found in Figures 9 and 10. This suggests that the core region in BL Lac is threaded by a large-scale helical magnetic field. A more detailed comparison between our observations and specific RMHD simulations using the estimated parameters for BL Lac is underway and will be published elsewhere.

4.2. Pattern of Recollimation Shocks

The location of the stationary feature ~ 0.26 mas from the core (see Section 3.1) marks a clear transition in the RM and polarization vectors between the core area and the remainder of the jet in BL Lac. Figure 9 shows a localized region of enhanced RM, reaching values of the order of -2200 ± 300 rad m^{-2}, and a Faraday rotation corrected EVPA of $-40° \pm 8°$. χ_0, therefore, becomes perpendicular to the local jet direction, suggesting a dominant component of the magnetic field that is aligned with the jet. Downstream of this location, χ_0 rotates so that the magnetic field remains predominantly aligned with the local jet direction up to a distance of ~ 1 mas from the core.

Further downstream polarization is detected again in a region at a distance of ~ 3 mas from the core, corresponding to the location of components K6 and K7 (see Figure 5). This area has a mean RM and χ_0 of -320 ± 140 rad m^{-2} and $14° \pm 6°$, respectively. The polarization vectors are approximately parallel to the jet in this area, thereby suggesting that the magnetic field is predominantly perpendicular to the jet. This would be in agreement with a helical magnetic field in which the toroidal component dominates over the poloidal one, although other scenarios, like a plane perpendicular shock, cannot be ruled out.

Considering that the polarization properties in the core area and components K6 and K7 suggest that the jet in BL Lac is threaded by a helical magnetic field, the different polarization structure associated with the stationary feature at ~ 0.26 mas from the core suggests that it may correspond to a rather

Table 3
Gaussian Model Fits for the VLBA-BU-BLAZAR 43 GHz Data

Epoch (year)	Flux (Jy)	Distance (mas)	PA (°)	Size (mas)
2013.96	1.620 ± 0.087	…	…	0.044 ± 0.005
	2.100 ± 0.111	0.096 ± 0.005	−174 ± 5	0.062 ± 0.006
	0.620 ± 0.039	0.285 ± 0.005	178 ± 1	0.087 ± 0.007
	0.227 ± 0.021	0.425 ± 0.014	179 ± 2	0.132 ± 0.005
	0.049 ± 0.010	1.260 ± 0.123	−167 ± 6	0.370 ± 0.019
	0.084 ± 0.016	1.660 ± 0.057	−170 ± 2	0.256 ± 0.012
	0.129 ± 0.020	2.590 ± 0.100	−173 ± 2	0.507 ± 0.025
	0.097 ± 0.020	3.790 ± 0.300	−166 ± 6	1.390 ± 0.070
2014.05	0.547 ± 0.028	…	…	<0.005
	1.040 ± 0.059	0.124 ± 0.005	−170 ± 2	0.063 ± 0.005
	1.110 ± 0.063	0.304 ± 0.005	−179 ± 1	0.104 ± 0.005
	0.168 ± 0.018	0.443 ± 0.018	178 ± 2	0.140 ± 0.007
	0.097 ± 0.017	1.530 ± 0.078	−169 ± 3	0.356 ± 0.018
	0.054 ± 0.011	1.960 ± 0.100	−168 ± 3	0.322 ± 0.016
	0.043 ± 0.009	2.480 ± 0.084	−176 ± 2	0.255 ± 0.012
	0.105 ± 0.019	2.990 ± 0.150	−172 ± 3	0.652 ± 0.033
2014.15	0.785 ± 0.045	…	…	0.028 ± 0.005
	0.735 ± 0.043	0.113 ± 0.005	−166 ± 3	0.048 ± 0.005
	0.434 ± 0.030	0.310 ± 0.006	−176 ± 1	0.091 ± 0.005
	0.070 ± 0.015	0.535 ± 0.054	172 ± 6	0.224 ± 0.011
	0.010 ± 0.003	1.050 ± 0.088	172 ± 5	0.126 ± 0.007
	0.021 ± 0.005	1.390 ± 0.087	−179 ± 4	0.182 ± 0.010
	0.058 ± 0.015	1.580 ± 0.092	−170 ± 3	0.318 ± 0.016
	0.065 ± 0.016	1.960 ± 0.100	−170 ± 3	0.357 ± 0.018
	0.037 ± 0.010	2.520 ± 0.130	−175 ± 3	0.332 ± 0.016
	0.133 ± 0.020	3.180 ± 0.160	−172 ± 3	0.755 ± 0.038
2014.34	1.450 ± 0.078	…	…	0.026 ± 0.005
	1.510 ± 0.082	0.140 ± 0.005	−161 ± 2	0.049 ± 0.006
	1.290 ± 0.071	0.297 ± 0.005	−162 ± 1	0.054 ± 0.007
	0.739 ± 0.045	0.335 ± 0.006	−172 ± 1	0.113 ± 0.006
	0.027 ± 0.007	0.658 ± 0.022	176 ± 1	0.031 ± 0.005
	0.013 ± 0.003	1.120 ± 0.113	171 ± 6	0.175 ± 0.008
	0.030 ± 0.008	1.310 ± 0.071	178 ± 3	0.184 ± 0.010
	0.111 ± 0.018	1.640 ± 0.077	−176 ± 3	0.374 ± 0.020
	0.025 ± 0.006	2.290 ± 0.100	−167 ± 3	0.224 ± 0.011
	0.040 ± 0.010	2.650 ± 0.110	−173 ± 2	0.305 ± 0.015
	0.141 ± 0.021	3.670 ± 0.200	−171 ± 3	0.967 ± 0.048
2014.47	0.991 ± 0.053	…	…	<0.005
	0.902 ± 0.052	0.148 ± 0.005	−165 ± 2	0.058 ± 0.005
	1.180 ± 0.066	0.335 ± 0.005	−164 ± 1	0.066 ± 0.005
	0.055 ± 0.011	0.437 ± 0.015	−156 ± 1	0.047 ± 0.006
	0.104 ± 0.017	0.634 ± 0.082	−177 ± 7	0.383 ± 0.019
	0.030 ± 0.007	0.961 ± 0.070	167 ± 4	0.176 ± 0.009
	0.049 ± 0.012	1.190 ± 0.060	174 ± 3	0.202 ± 0.010
	0.084 ± 0.016	1.520 ± 0.080	−177 ± 3	0.332 ± 0.026
	0.047 ± 0.012	1.980 ± 0.200	−175 ± 6	0.524 ± 0.023
	0.044 ± 0.011	2.660 ± 0.170	−173 ± 4	0.459 ± 0.023
	0.128 ± 0.021	3.740 ± 0.220	−171 ± 3	0.960 ± 0.048

Note. Tabulated data correspond to flux density, distance and position angle from the core, and size. Errors in the model-fit parameters for each component are estimated based on its brightness temperature following Casadio et al. (2015).

particular jet feature. This would be in agreement with claims by Cohen et al. (2015), and references therein, in which these authors conclude that this stationary feature corresponds to a recollimation shock, downstream of which new superluminal components appear due to the propagation of Alfvén waves

triggered by the swing in its position, in a similar way as exciting a wave on a whip by shaking the handle.

Previous multiwavelength observations of BL Lac suggest that the core may also correspond to a recollimation shock (Marscher et al. 2008). In that case, we can hypothesize that the upstream component found in our *RadioAstron* observation (see Figure 5 and Table 2) is located at the jet apex, so that the distance at which the first recollimation shock takes place, associated with the core, would be ~40 μas. If so, the jet in BL Lac would contain a set of three recollimation shocks, spaced at progressively larger distances of approximately 40, 100, and 250 μas.

To investigate such a pattern of recollimation shocks as possibly observed in BL Lac, we have performed two-dimensional special RMHD simulations in cylindrical geometry using the RAISHIN code (Mizuno et al. 2006, 2011). The initial set-up follows Gómez et al. (1997) and Mizuno et al. (2015), in which a preexisting over-pressured flow is established across the simulation domain. We choose a rest-mass density ratio between the jet and ambient medium of $\eta = \rho_j/\rho_a = 5 \times 10^{-3}$ with $\rho_a = 1.0\rho_0$, initial jet Lorentz factor $\gamma_j = 3$, and local Mach number $M_s = 1.69$. The gas pressure in the ambient medium decreases with axial distance from the jet base following $p_{g,a}(z) = p_{g,0}/[1 + (z/z_c)^n]^{m/n}$, where $z_c = 60R_j$ is the gas pressure scale height in the axial direction, R_j is the jet radius, $n = 1.5$, $m = 2.3$, and $p_{g,0}$ is in units of $\rho_0 c^2$ (e.g., Gómez et al. 1995, 1997; Mimica et al. 2009). We assume that the jet is initially uniformly over-pressured with $p_{g,j} = 1.5p_{g,a}$. We consider a force-free helical magnetic field with a weak magnetization $B_0 = 0.05$ (in units of $\sqrt{4\pi\rho_0 c^2}$) and constant magnetic pitch $P_0 = RB_z/R_jB_\phi = 1/2$, where B_z and B_ϕ are the poloidal and toroidal magnetic field components, so that smaller P_0 refers to increased magnetic helicity.

Overexpansions and overcontractions caused by inertial overshooting past equilibrium of the jet lead to the formation of a pattern of standing oblique recollimation shocks and rarefactions, whose strength and spacing are governed by the external pressure gradient (see Figure 11). The jet is accelerated and conically expanded slightly by the propegation of rarefaction (e.g. Aloy & Rezzolla 2006; Mizuno et al. 2008) and the gas gradient force, reaching a maximum jet Lorentz factor of ~8. The jet radius expands from the initial $R_j = 1$ at the jet base to $R_j = 1.5$ at $z = 60R_j$, yielding an opening angle of $\theta_j = \arctan(0.5R_j/60R_j) \sim 0°.48$. The recollimation shocks are located at progressively larger axial distances of ~$7R_j$, ~$20R_j$, and ~$42R_j$. The relative distances between the second and third shocks with respect to the first one are ~2.9 and ~6, which roughly match those observed in BL Lac.

The output from the RMHD simulation is used as input to compute the radio continuum synchrotron emission map shown in Figure 12. Following Gómez et al. (1995), the internal energy is distributed among the non-thermal electrons using a power law $N(E)dE = N_0E^{-p}dE$, with $p = 2.4$. The emission is computed for a viewing angle of 10° and at an optically thin observing frequency, integrating the synchrotron transfer equations along the line of sight (e.g., Gómez et al. 1997). The pattern of recollimation shocks seen in Figure 11 leads to a set of knots in the total and linearly polarized intensity. The EVPAs in the knots are perpendicular to the jet direction, in agreement with the observations of component K2 in BL Lac. We note, however, that our RMHD simulations consider an

already formed and collimated jet, and therefore do not provide an accurate account of the jet formation region, close to where the other two innermost recollimation shocks are located.

Finally, although our simulations are in general agreement with the pattern of recollimation shocks observed in BL Lac, further numerical simulations, in progress, are required to better constrain the jet parameters of the model, such as the Lorentz factor, Mach number, gradient in external pressure, magnetic field helicity/strength, and viewing angle.

5. SUMMARY

RadioAstron provides the first true full-polarization capabilities for space VLBI observations on baselines longer than the Earth's diameter, opening the possibility to achieve unprecedentedly high angular resolution in astronomical imaging. In this paper, we present the first polarimetric space VLBI observations at 22 GHz, obtained as part of our *RadioAstron* KSP designed to probe the innermost regions of AGNs and their magnetic fields in the vicinity of the central black hole.

The jet of BL Lac was observed in 2013 November 10 at 22 GHz with *RadioAstron* including a ground array of 15 radio telescopes. The instrumental polarization of the SRT was found to remain within 9% (5% for LCP), demonstrating its polarization capabilities for *RadioAstron* observations at its highest observing frequency of 22 GHz.

The phasing of a group of ground-based antennas allowed us to obtain reliable ground-space fringe detections up to projected baseline distances of 7.9 Earth diameters in length. Polarization images of BL Lac are obtained with a maximum angular resolution of 21 μas, the highest achieved to date.

Analysis of the 43 GHz data from the VLBA-BU-BLAZAR monitoring program, covering from 2013 November to 2014 June, reveals a new component ejected near the epoch of our *RadioAstron* observations, confirmed also by flares in the optical and γ-ray light curves. This new component appears in the *RadioAstron* image as a knot 41 ± 3 μas upstream of the radio core, in agreement with previous detections of upstream emission in BL Lac (Marscher et al. 2008). The radio core would then correspond to a recollimation shock at $\sim$40 μas from the jet apex, part of a pattern that also includes two other recollimation shocks at approximately 100 and 250 μas. Our RMHD simulations show that such a pattern of recollimation shocks, spaced at progressively larger distance, is expected when the jet propagates through an ambient medium with a decreasing pressure gradient.

Polarization is detected in two components within the innermost 0.5 mas of the core, and in some knots $\sim$3 mas downstream. We have combined the *RadioAstron* 22 GHz image with ground-based observations at 43 and 15 GHz to compute an RM map. Analysis of the core area reveals a gradient in RM and Faraday-corrected EVPA that depends on the position angle with respect to the core, in a similar way as found in the jet of 3C 454.3 (Zamaninasab et al. 2013) and in agreement with numerical RMHD simulations of jets threaded by a helical magnetic field (Broderick & McKinney 2010; Porth et al. 2011).

The stationary feature $\sim$250 μas from the core contains an enhanced RM and marks a temporary transition in polarization vectors, in which the magnetic field becomes predominantly aligned with the local direction of the jet, in agreement with our RMHD simulations.

We obtain a lower limit for the observed brightness temperature of the unresolved core in our *RadioAstron* image of 2×10^{13} K. Using previous estimates of the Doppler factor of $\delta = 7.2$, we calculate an intrinsic brightness temperature in excess of 3×10^{12} K, implying that the jet in BL Lac is not in equipartition of energy between the magnetic field and emitting particles and also suggesting that its Doppler factor is significantly underestimated.

RadioAstron polarimetric space VLBI observations provide a unique tool to study the innermost regions of AGN jets and their magnetic fields with unprecedented high angular resolutions. This will be investigated in a series of papers, containing results from our *RadioAstron* KSP, which studies a sample of powerful, highly polarized, and γ-ray bright blazars.

REFERENCES

Alloy, M. M., & Rezzolla, L. 2006, ApJL, 640, L115
Asada, K., Inoue, M., Uchida, Y., et al. 2002, PASJ, 54, L39
Benford, G., & Tzach, D. 2000, MNRAS, 317, 497
Blandford, R. D., & Payne, D. G. 1982, MNRAS, 199, 883
Blandford, R. D., & Znajek, R. L. 1977, MNRAS, 179, 433
Broderick, A. E., & McKinney, J. C. 2010, ApJ, 725, 750
Bruni, G., Anderson, J., Alef, W., Lobanov, A. P., & Zensus, A. J. 2014, in Proc. 12th European VLBI Network Symp. 119, Space VLBI with *RadioAstron*: New Correlator Capabilities at MPIFR, ed. A. Tarchi, M. Giroletti, & L. Feretti (POS), 119
Casadio, C., Gómez, J. L., Jorstad, S. G., et al. 2015, ApJ, 813, 51

Cohen, M. H., Meier, D. L., Arshakian, T. G., et al. 2014, ApJ, 787, 151
Cohen, M. H., Meier, D. L., Arshakian, T. G., et al. 2015, ApJ, 803, 3
Croke, S. M., & Gabuzda, D. C. 2008, MNRAS, 386, 619
Ford, H. A., Anderson, R., Belousov, K., et al. 2014, Proc. SPIE, 9145, 91450B
Gabuzda, D. C., & Gómez, J. L. 2001, MNRAS, 320, L49
Gómez, J. L., Alberdi, A., Marcaide, J. M., Marscher, A. P., & Travis, J. P. 1994, A&A, 292, 33
Gómez, J. L., & Marscher, A. P. 2000, ApJ, 530, 245
Gómez, J. L., Martí, J. M., Marscher, A. P., Ibáñez, J. M., & Alberdi, A. 1997, ApJL, 482, L33
Gómez, J. L., Marti, J. M. A., Marscher, A. P., Ibanez, J. M. A., & Marcaide, J. M. 1995, ApJL, 449, L19
Hovatta, T., Lister, M. L., Aller, M. F., et al. 2012, AJ, 144, 105
Hovatta, T., Valtaoja, E., Tornikoski, M., & Lähteenmäki, A. 2009, A&A, 494, 527
Jorstad, S. G., Marscher, A. P., Lister, M. L., et al. 2005, AJ, 130, 1418
Jorstad, S. G., Marscher, A. P., Stevens, J. A., et al. 2007, AJ, 134, 799
Jukes, J. D. 1967, Natur, 216, 461
Kardashev, N. S., Khartov, V. V., Abramov, V. V., et al. 2013, ARep, 57, 153
Kellermann, K. I. 2002, PASA, 19, 77
Kellermann, K. I., & Pauliny-Toth, I. I. K. 1969, ApJL, 155, L71
Kogan, L. 1996, VLBA Scientific Memo # 13
Kovalev, Y. A., Vasil'kov, V. I., Popov, M. V., et al. 2014, CosRe, 52, 393
Kovalev, Y. Y., Kellermann, K. I., Lister, M. L., et al. 2005, AJ, 130, 2473
Kovalev, Y. Y., Lobanov, A. P., Pushkarev, A. B., & Zensus, J. A. 2008, A&A, 483, 759
Lähteenmäki, A., Valtaoja, E., & Wiik, K. 1999, ApJ, 511, 112
Laing, R. A. 1981, ApJ, 248, 87
Leppanen, K. J., Zensus, J. A., & Diamond, P. J. 1995, AJ, 110, 2479
Levy, G. S., Linfield, R. P., Ulvestad, J. S., et al. 1986, Sci, 234, 187
Lind, K. R., Payne, D. G., Meier, D. L., & Blandford, R. D. 1989, ApJ, 344, 89
Lister, M. L., Aller, M. F., Aller, H. D., et al. 2013, AJ, 146, 120
Lobanov, A. 2015, A&A, 574, A84
Lobanov, A. P. 1998, A&A, 330, 79
Lobanov, A. P., Gómez, J. L., Bruni, G., et al. 2015, A&A, 583, A100
Lobanov, A. P., & Zensus, J. A. 2001, Sci, 294, 128
Marscher, A. P., Jorstad, S. G., D'Arcangelo, F. D., et al. 2008, Natur, 452, 966
Marscher, A. P., Jorstad, S. G., Gómez, J. L., et al. 2002, Natur, 417, 625
McKinney, J. C., & Blandford, R. D. 2009, MNRAS, 394, L126
Meier, D. L. 2013, in EPJ Web of Conf. 61, In The Innermost Regions of Relativistic Jets and Their Magnetic Fields, The Phoenix Fire Model for Jet Creation: The Role of Magnetic Fields in the Production and Propegation of Relativistic Jets, ed. J. L. Gómez (London: EDP Sciences), 01001
Mimica, P., Aloy, M. A., Agudo, I., et al. 2009, ApJ, 696, 1142
Mizuno, Y., Gómez, J. L., Nishikawa, K.-I., et al. 2015, ApJ, 809, 38
Mizuno, Y., Hardee, P., Hartmann, D. H., Nishikawa, K.-I., & Zhang, B. 2008, ApJ, 672, 72
Mizuno, Y., Hardee, P. E., & Nishikawa, K.-I. 2011, ApJ, 734, 19
Mizuno, Y., Nishikawa, K.-I., Koide, S., Hardee, P., & Fishman, G. J. 2006, arXiv:astro-ph/0609004
Mutel, R. L., & Denn, G. R. 2005, ApJ, 623, 79
O'Sullivan, S. P., & Gabuzda, D. C. 2009, MNRAS, 393, 429
Pashchenko, I. N., Kovalev, Y. Y., & Voitsik, P. A. 2015, CosRe, 53, 199
Planck Collaboration, Ade, P. A. R., Aghanim, N., et al. 2014, A&A, 571, A16
Porth, O., Fendt, C., Meliani, Z., & Vaidya, B. 2011, ApJ, 737, 42
Pushkarev, A. B., Hovatta, T., Kovalev, Y. Y., et al. 2012, A&A, 545, 113
Pushkarev, A. B., & Kovalev, Y. Y. 2015, MNRAS, 452, 4274
Readhead, A. C. S. 1994, ApJ, 426, 51
Shepherd, M. C. 1997, in ASP Conf. Ser. 125, Astronomical Data Analysis Software and Systems VI, ed. G. Hunt, & H. E. Payne (San Francisco, CA: ASP), 77
Sokolovsky, K. V., Kovalev, Y. Y., Pushkarev, A. B., & Lobanov, A. P. 2011, A&A, 532, 38
Stirling, A. M., Cawthorne, T. V., Stevens, J. A., et al. 2003, MNRAS, 341, 405
Walker, R. C., Dhawan, V., Romney, J. D., Kellermann, K. I., & Vermeulen, R. C. 2000, ApJ, 530, 233
Woo, J.-H., & Urry, C. M. 2002, ApJ, 579, 530
Zamaninasab, M., Clausen-Brown, E., Savolainen, T., & Tchekhovskoy, A. 2014, Natur, 510, 126
Zamaninasab, M., Savolainen, T., Clausen-Brown, E., et al. 2013, MNRAS, 436, 3341
Zavala, R. T., & Taylor, G. B. 2003, ApJ, 589, 126